The Astrophysical Journal, 944:228 (14pp), 2023 February 20 https://doi.org/10.3847/1538-4357/acb8bc

Structure and Kinematics of Sh2-138—A Distant Hub-filament System in the Outer Galactic Plane

Kshitiz K. Mallick[1], Lokesh K. Dewangan[2], Devendra K. Ojha[3], Tapas Baug[4], and Igor I. Zinchenko[5]
[1] Aryabhatta Research Institute of Observational Sciences (ARIES), Manora Peak, Nainital, 263002, India; kshiitiz@gmail.com
[2] Physical Research Laboratory, Navrangpura, Ahmedabad 380009, India
[3] Department of Astronomy and Astrophysics, Tata Institute of Fundamental Research, Homi Bhabha Road, Mumbai 400005, India
[4] S.N. Bose National Centre for Basic Sciences, Block JD, Sector III, Salt Lake, Kolkata 700106, West Bengal, India
[5] Institute of Applied Physics of the Russian Academy of Sciences, 46 Ul'yanov str., 603950 Nizhny Novgorod, Russia
Received 2022 January 14; revised 2023 January 31; accepted 2023 January 31; published 2023 February 28

Abstract

We present a molecular line study of the Sh2-138 (IRAS 22308+5812) *hub-filament* system with the aim of investigating its structure and kinematics. Archival CO molecular line data from the Canadian Galactic Plane Survey (CO(J = 1–0)) for the wider region ($\sim 50' \times 50'$) and the James Clerk Maxwell Telescope (CO(3–2), ^{13}CO(3–2), and C^{18}O(3–2)) for the central portion ($\sim 5' \times 5'$) have been utilized. Analysis of the CO(1–0) spectra for the extended region in conjunction with the identification of the hub and filament using a column density map and the *getsf* tool, respectively, reveals a complex structure with the spectral extraction for the central position displaying multiple velocity components. Based on the Herschel 70 μm warm dust emission, one of the filaments in the extended region was inferred to be associated with active star formation, and is host to a Bolocam 1.1 mm clump of $\sim 1606\,M_{\odot}$. An integrated intensity map of ^{13}CO(3–2) emission, constructed from clumps detected at above 5σ in position–position–velocity space, reveals three filamentary structures (labeled the western filament (W-f), southwestern filament (SW-f), and southeast filament (SE-f)) in the central portion. Velocity gradients observed in ^{13}CO(3–2) position–velocity slices point to longitudinal gas flow along the filaments into the central region. Filaments W-f, SW-f, and SE-f were calculated to have observed line masses of $\sim$32, 33.5, and $50\,M_{\odot}$ pc^{-1}, respectively. The cloud was found to be dominated by supersonic and nonthermal motions, with high Mach numbers ($\gtrsim$3) and a low thermal-to-nonthermal pressure ratio ($\sim$0.01–0.1).

Unified Astronomy Thesaurus concepts: Interstellar medium (847); Interstellar filaments (842); Interstellar molecules (849); H II regions (694); Millimeter astronomy (1061); Star formation (1569); Massive stars (732)

1. Introduction

Understanding the evolutionary sequence of high-mass stars ($\geqslant 8\ M_{\odot}$) is an area of ongoing development in astronomy (Zinnecker & Yorke 2007). Observations indicate that massive stars are generally found in the center of embedded young stellar clusters in giant molecular clouds (Kumar et al. 2006; Beuther et al. 2007; Portegies Zwart et al. 2010). The Lyman continuum radiation output of such stars ionizes the natal cloud leading to the formation of H II regions, which evolve from a compact to a classical phase. Observations in the past few decades have led to an empirical view that high-mass stars, and dense and massive cold cloud structures could be analogous to prestellar cores in low-mass stars (Motte et al. 2018). Infrared dark clouds—seen in absorption against mid-infrared emission (such as observed by Spitzer)—are promising sites of such dense cloud cores, with some resembling the *hub-filament* model of Myers (2009) seen in emission in far-infrared observations by Herschel. According to Inutsuka & Miyama (1997), filamentary features represent an important step in the evolutionary life of a molecular cloud as it progresses toward fragmentation into dense clumps. The study by Kumar et al. (2020) has even concluded that almost all massive star formation occurs in the hubs and suggested a *filaments to clusters* paradigm.

It thus becomes imperative to study young stellar clusters hosting high-mass stars, with the presence of a photodissociated region being their typical signature. Sh2-138 (or G105.6270 +00.3388; $l \sim 105.^{\circ}6270$, $b \sim +0.^{\circ}3392$), associated with the IRAS source (IRAS 22308+5812) in Cepheus, is one such Galactic optical H II region. The extent of the ionized region and the parameters derived (electron density, emission measure, etc) from radio continuum observations (Fich 1993; Martín-Hernández et al. 2002) have shown it to be a classical H II region (Kurtz 2002). Early optical and near-infrared observations by Deharveng et al. (1999) found four O/B-type stars in a similar layout as that of the Orion Trapezium cluster. The multiwavelength study of Baug et al. (2015) revealed further compact radio clumps, as well as provided age and spectral type estimates of the cluster of O/B stars. Their analyses found an isolated cluster of young stellar objects—with a mean age of $\sim$1 Myr—centered on the location of the IRAS source lying at the junction of filaments. The massive star(s) seem to be driving molecular outflows in the region (Qin et al. 2008), and a possible (weak) water maser detection (Cesaroni et al. 1988; Palagi et al. 1993; Wouterloot et al. 1993) is likely an outcome of this (Fish 2007), though more recent studies (Urquhart et al. 2011) suggest non-detection. It should however be noted that there is an absence of methanol masers in the region (Slysh et al. 1999; Szymczak et al. 2000). Early molecular observations of the region in CO (Dickinson et al. 1974; Blitz et al. 1982; Wouterloot & Brand 1989), HCN (Burov et al. 1988), HCO+ (Zinchenko et al. 1990; Yoo et al. 2018), NH_3 (Harju et al. 1993; Urquhart et al. 2011), CS (Bronfman et al. 1996), and

Table 1
Data Used in This Work

Data Source	Line/Wavelength	Spatial Resolution	Channel Width	Reference
		Spectral Data Products		
CGPS	CO(1–0)	∼100.″44	∼0.82 km s^{-1}	Taylor et al. (2003)
JCMT archive	CO(3–2)	∼14″	∼0.42 km s^{-1}	Buckle et al. (2009)
JCMT archive	^{13}CO(3–2), C^{18}O(3–2)	∼14″	∼0.05 km s^{-1} (0.5 km s^{-1} for rebinned cubes)	Buckle et al. (2009)
		Imaging Products		
ViaLactea maps	⋯	∼12″	⋯	Molinari et al. (2010)
Herschel archive	70 μm	∼5″	⋯	Poglitsch et al. (2010)
	250 μm, 350 μm	∼18″, ∼25″	⋯	Griffin et al. (2010)
NVSS	1.4 GHz	∼45″	⋯	Condon et al. (1998)
BGPS	1.1 mm	∼33″	⋯	Aguirre et al. (2011)

other species' isotopologues (Johansson et al. 1994) have been able to detect the spectra of the molecular cloud centered in the ∼−53 to −52 km s^{-1} range. More recent higher-resolution CO observations (Brunt et al. 2003; Kerton & Brunt 2003) have found multiple velocity components associated with the molecular cloud. The multitude of molecular line studies have probed different physical conditions in the cloud, but at specific locations (mostly on the coordinate of the IRAS source) and have not looked at the spatial variation of the spectra (and thus the physical conditions) in the wider region, though this could be partly due to the low resolution of some of the studies. The relatively comprehensive study of Baug et al. (2015) focused on the optical and near-infrared study of stellar sources and the ionized morphology. Also, their inference from the Herschel column density map that this region lies at the junction of filaments makes it natural to explore the structure of the filamentary features in molecular line transitions. This paper aims to fulfill this void (partly, in various transitions of CO isotopologues) for a better understanding of the interplay of the (massive) stellar cluster and the hub-filament system (HFS) in the Sh2-138 H II region.

Deharveng et al. (1999) use a distance of 5.0 ± 1.0 kpc for the Sh2-138 H II region in their analysis based on the average distance to nearby compact H II regions, though their kinematic distance calculation from V_{LSR}(CO) suggests a value in the range 5.45–5.9 kpc. Anderson et al. (2014) also calculated a value of ∼5.8 kpc based on the velocity from NH_3 spectrum. According to Blitz et al. (1982), H II regions with similar velocities (∼−53 km s^{-1}) near Sh2-138, namely, Sh2-148 and Sh2-149, have distances of ∼5.5 and 5.4 kpc, respectively. Similar distance estimates have been used by Wouterloot & Brand (1989, ∼5.7 kpc) and Johansson et al. (1994, ∼6.0 kpc) using a mean of kinematic distance and the estimate from the size–line width relation; see Martín-Hernández et al. (2002, ∼5.5 kpc); Baug et al. (2015, ∼5.7 kpc); and Zhang et al. (2020, ∼5.7 kpc). For the purpose of this paper, we thus adopt the distance of 5.7 kpc in Baug et al. (2015).

This paper is organized as follows. In Section 2, we list the various data sets used in this paper. This is followed by an analysis and our results in Section 3, where the large-scale view of the region is examined (Section 3.1) and the kinematics of the molecular gas in the central region is presented (Section 3.2) A discussion of our results follows in Section 4, and finally, we conclude with a summary of major findings in Section 5.

2. Data Used

Table 1 provides a summary of the data sets used in this paper. A brief description of the salient parts is provided in the following part of this section.

Archival spectral cubes for ^{12}CO(1–0) (2.6 mm) emission produced by the Canadian Galactic Plane Survey (CGPS) Consortium (Taylor et al. 2003) were procured for the region. The CGPS cubes are based on the Five College Radio Astronomy Observatory outer galaxy survey (Heyer et al. 1998) regridded to a pixel scale of 18″ and channel width of 0.824 km s^{-1}. The spectral cube data, given in radiation temperature scale (i.e., T_R^*), has a spatial resolution of 100.″44.

Besides CGPS, archival James Clerk Maxwell Telescope (JCMT) observations of the Sh2-138 (G105.6270+00.3388) region were downloaded using the CADC[6] data repository. Calibrated spectral cubes for the three molecular lines—CO(3–2) (rest frequency = 345.79599 GHz; Proposal ID: M07AU08; Int. time: 17.983 s), ^{13}CO(3–2) (rest frequency = 330.587960 GHz; Proposal ID: M08BU18; Int. time: 48.896 s), and C^{18}O(3–2)(rest frequency = 329.330545 GHz; Proposal ID: M08BU18; Int. time: 48.808 s)—observed using the Heterodyne Array Receiver Program/Auto-Correlation Spectral Imaging System (HARP/ACSIS; Buckle et al. 2009) spectral imaging system were retrieved. The $J = 3$–2 transition traces gas at a higher critical density (Buckle et al. 2010, ∼$10^{4–5}$ cm^{-3}) than the CGPS CO(J = 1–0) data whose critical density is of the order of ∼ 10^3 cm^{-3} (Bolatto et al. 2013; Shirley 2015). The temperature scale used for the pixel brightness units is T_A^* (antenna temperature) for all three spectral cubes. Basic processing for the purpose of our analysis involved the conversion of spectral axis units from frequency to velocity scale, and the coordinate system to Galactic from FK5. Both the ^{13}CO(3–2) and C^{18}O(3–2) JCMT cubes had a channel width of ∼ 0.05 km s^{-1}, with a mean rms noise of ∼0.96 ± 0.45 and 1.3 ± 0.7 K, respectively. While we use these cubes for spectra analysis due to their high-velocity resolution, for the detection of spatial structures, we

[6] https://www.cadc-ccda.hia-iha.nrc-cnrc.gc.ca/en/search/

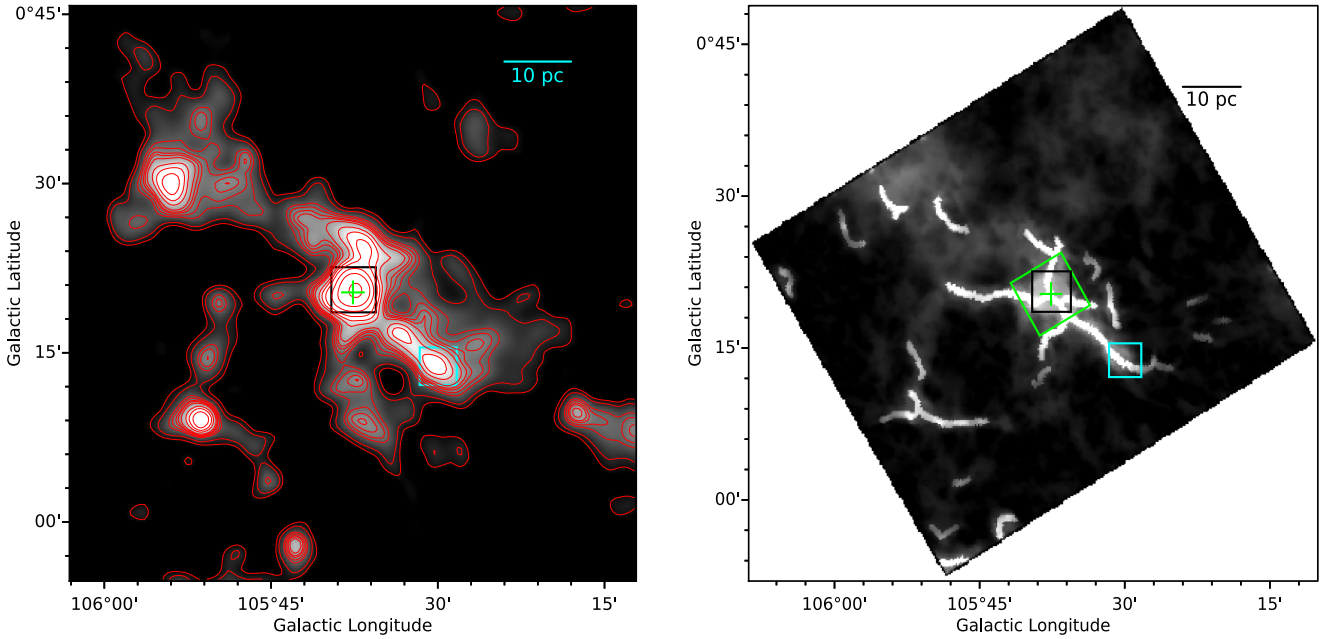

Figure 1. (Left) CO(1–0) integrated-intensity map in the [−62.5, −41] km s^{-1} velocity range. Contours have also been drawn (at 5, 7, 11, 12.5, 14, 15, 16.5, 20, 23, 27, 35, 45, and 65 K km s^{-1}) for clarity of the features. (Right) Herschel 350 μm image with overlaid skeletons of filaments identified by *getsf*. The black box denotes the central portion where CO(1–0) spectrum has been extracted. The cyan box marks the CO clump, which also (i.e., apart from the central region) corresponds to $N(H_2) \geqslant 10^{22}$ cm^{-2} (see Figure 2). The green plus symbol shows the location of IRAS 22308+5812, and the green box on the 350 μm image shows the field of view of the JCMT analysis (see Section 3.2).

averaged and rebinned both these cubes along the spectral axis to 0.5 km s^{-1} channels. The resultant rebinned cubes had a reduced mean rms noise of 0.30 ± 0.14 and 0.41 ± 0.23 K for ^{13}CO(3–2) and C^{18}O(3–2), respectively. The above tasks were implemented using STARLINK KAPPA (Currie et al. 2014) package commands, such as "wcsattrib" and "sqorst." The CO(3–2) cube—which had a native channel width of ∼0.42 km s^{-1} and a mean rms noise of 0.53 ± 0.2 K—was mainly used to examine the morphology of the region. Each of the images in the cubes has a pixel scale of ∼7.″3, and a beam size of ∼14″ (Buckle et al. 2009, 2010; Davis et al. 2010; Graves et al. 2010), which is equivalent to ∼0.4 pc at a distance of 5.7 kpc.

For the purpose of examining the column density and temperature of the region, we retrieved the publicly available ViaLactea Herschel maps of them[7] (Molinari et al. 2010). These maps have been generated by applying the Bayesian point-process procedure (Marsh et al. 2015) to Hi-Gal survey images (Marsh et al. 2017). The pixel scale of ∼6″ and a resolution of ∼12″ makes them suitable to examine in conjunction with the JCMT data. Finally, the Herschel Photodetector Array Camera and Spectrometer (PACS; Poglitsch et al. 2010) 70 μm image and Spectral and Photometric Imaging Receiver (SPIRE; Griffin et al. 2010) 250 and 350 μm images (Proposal: "OT2_smolinar_7") were retrieved from the archives for morphological examination and filament identification purposes.

3. Analysis and Results

3.1. Large-scale View of the Region

In this section, we explore the large-scale morphology as well as the HFS in the region. Figure 1 (left) shows the ^{12}CO(1–0) moment-0 (integrated-intensity) map of the larger region in the velocity range of [−62.5, −41] km s^{-1}. The central core has been marked with a black box and the IRAS source (IRAS 22308+5812) with a green plus symbol. Multiple filamentary structures can be seen emanating from this central core, with each of them harboring separate potential clumps of their own. To better understand the filamentary structure of the region, we used the *getsf* tool (version 211109) of Men'shchikov (2021). The tool, specially developed for Herschel images, decomposes an image into its structural components (sources and filaments) and separates them from their background. The method is fully automated and takes as input only one parameter from the user—the maximum size of the structure to extract. For our purpose, we used the Herschel 350 μm image, and set the maximum size of the filamentary structure to 550″ based on visual inspection. Figure 1 (right) shows the Herschel 350 μm image with the skeleton of filamentary structures identified by the *getsf* tool. It should be noted that the width associated with the skeletons on the image is only for visualization purposes. It can be seen that the structures that appear nearly contiguous in emission in the CO map (Figure 1 (left)) are detected as different (filamentary) structures as shown in Figure 1 (right). Figure 2 shows a zoomed-in view of Figure 1 (right) with overlaid column density contours from the ViaLactea map and the major axes of red and blue outflow lobes from Qin et al. (2008). According to the criteria of Myers (2009), the hub has a low aspect ratio, and can be defined in terms of column density as the region where $N(H_2) \gtrsim 10^{22}$ cm^{-2}. According to this definition, the hub region here (solid magenta contour in Figure 2) occurs at the location where there is a joining of multiple filaments. Some of the *getsf* filaments are also traced by a lower column density contour at 33×10^{20} cm^{-2}. However, the large-scale view of the region shows that the filament sizes have an order of magnitude of ∼10 pc. This is in contrast with nearby HFS,

[7] http://www.astro.cardiff.ac.uk/research/ViaLactea/

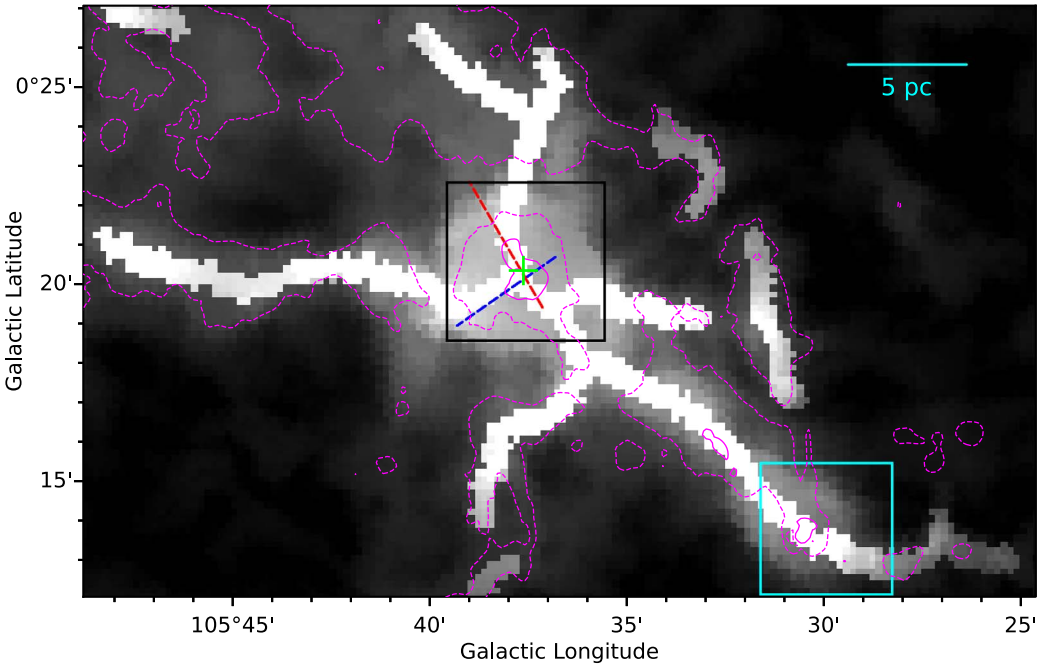

Figure 2. A zoomed-in view of Figure 1 (right). Magenta dashed and solid contours mark $N(H_2) = 33 \times 10^{20}$ and 10^{22} cm^{-2}, respectively, from the ViaLactea maps. Dashed blue and red lines mark the major axes of the blue and red outflow contours, respectively, from Qin et al. (2008). The rest of the symbols are the same as those in Figure 1.

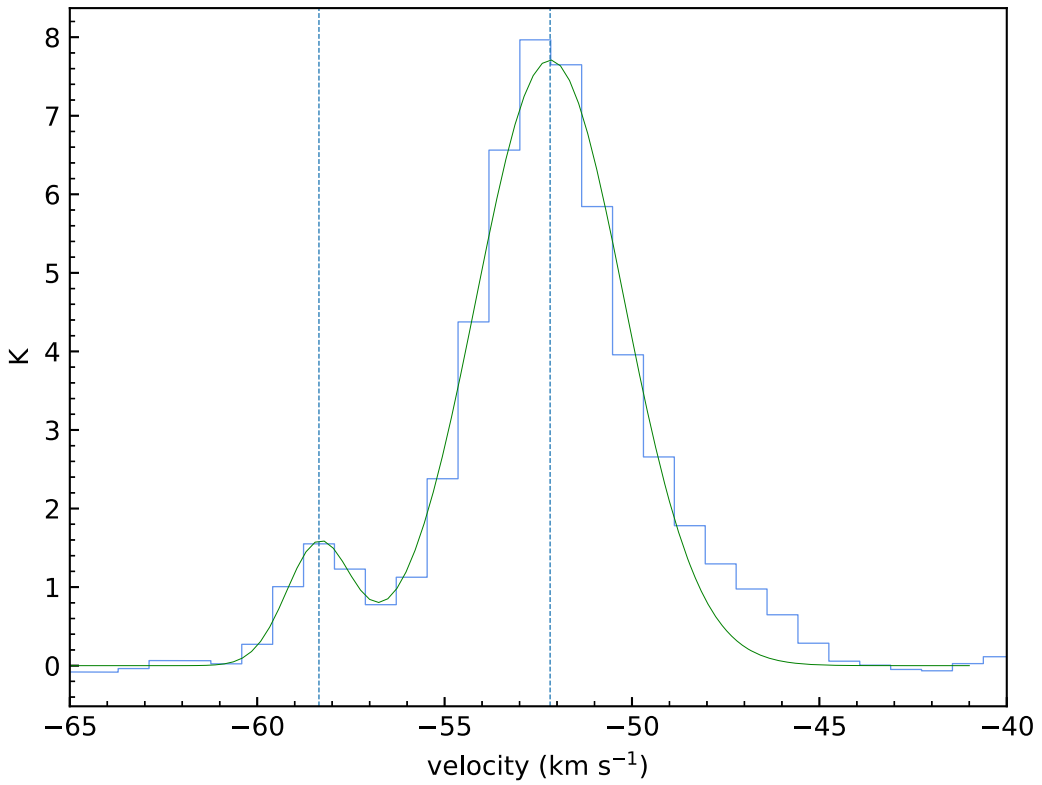

Figure 3. CO(1–0) spectrum at the central position marked in Figure 1 (left). The green curve shows the Gaussian fit, and dashed vertical lines mark the peak velocities of the two velocity components.

where filaments have been found to have sizes of the order of magnitude of ∼1 pc (Arzoumanian 2017; Arzoumanian et al. 2019). On the other hand, large filaments of sizes in tens of parsecs have also been recorded in the literature (Zucker et al. 2018; Hacar et al. 2022). Nevertheless, as discussed by Kumar et al. (2020), we would also like to add the caveat that higher-resolution studies of the region could resolve it into structures with hub/filament size scales similar to those of the nearby regions.

Figure 3 shows the ^{12}CO(1–0) line spectrum in the central region and the Gaussian fit to its components. The first velocity component is at $(v \pm \sigma)$ -58.4 ± 0.9 km s^{-1} with an amplitude

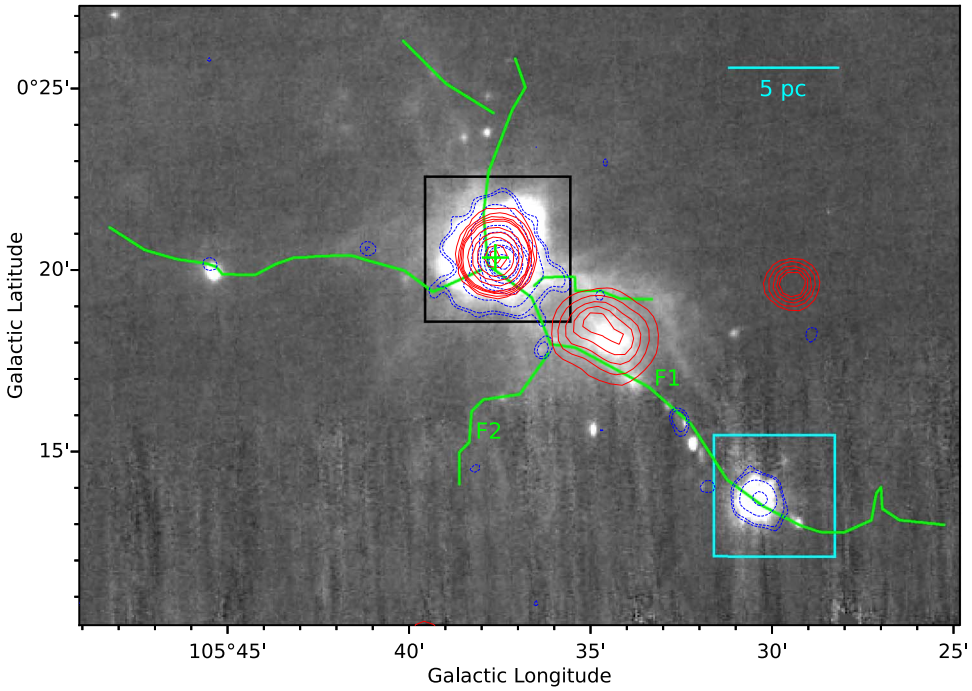

Figure 4. Herschel 70 μm image of the HFS. Bolocam 1.1 mm emission is shown in blue dashed contours at 0.08, 0.1, 0.2, 0.4, 0.5, 0.7, 0.9, 1.0, and 1.4 Jy beam^{-1}. Red contours (at 0.002, 0.004, 0.007, 0.01, 0.013, 0.04, 0.08, 0.15, 0.3, and 0.4 Jy beam^{-1}) are for the NVSS 1.4 GHz emission. Green lines mark the *getsf* filamentary skeletons (see Figure 2). The green cross shows the location of the IRAS source, and "F1" and "F2" are the labels for the two respective filaments. The central black box and the cyan box are the same as in Figure 2.

of 1.5 K, while the second component is at -52.2 ± 2.0 km s^{-1} with an amplitude of 7.7 K. These two different velocity components have been observed in earlier studies as well (Wouterloot & Brand 1989; Brunt et al. 2003; Kerton & Brunt 2003). It must be noted that CO(1–0) emission is regarded as optically thick and often self-absorbed. Hence, it is not used as a probe for the denser regions of the molecular cloud. For the central region, the stronger velocity component has a prominent broad wing toward the red side, which is probably an effect of the outflow.

Figure 4 shows the Herschel 70 μm image of the region, overlaid with filament skeletons from the *getsf* tool (Figure 2), smoothed Bolocam 1.1 mm contours (in blue), and NVSS 1.4 GHz contours (in red). 70 μm emission traces the warm dust emission due to stellar sources and is indicative of star formation in a region (Li et al. 2010; Calzetti 2013). It can be seen that along the filament marked "F1" on the image, there appears to be star formation activity, as evidenced by the presence of bright diffused emission along its length. To the slight west of the point where filament F1 joins filament F2, extended emission can be traced on the image, also seen in NVSS (red contours). The integrated flux density from the NVSS image was obtained to be 0.06 Jy, yielding a Lyman continuum flux of $\sim 10^{47.2}$ photons s^{-1} (Moran 1983), which in comparison with the tabulated values from Panagia (1973) (assuming a zero-age main sequence (ZAMS) single source) would suggest that a source of at least spectral type B0.5–B0 is required for the ionization of the region. Though no massive stars have been found located in the immediate vicinity of this diffused ionized region, it is possible that there could be embedded massive star formation at the junction of filaments F1 and F2. The presence of a 1.1 mm clump at this junction could be an affirmation of this.

Filament F1 also hosts a few Bolocam 1.1 mm emission clumps along its length, especially at its southwest corner, where there appears to be a massive clump (within the cyan box). We retrieved the integrated flux density from the Bolocam Galactic Plane Survey Catalog v2.1 (Ginsburg et al. 2013) from the IRSA[8] archive. Apart from the 1.1 mm emission in the central region (associated with IRAS 22308 +5812), the catalog contains only the clump in the southwest in our field of view. Other contours depicting 1.1 mm emission might not have been included due to not meeting the catalog criteria (Ginsburg et al. 2013). Nevertheless, it is relevant to note their presence along the filaments. The retrieved integrated flux density was used to calculate the core total mass of gas and dust using the following formula (Hildebrand 1983; Enoch et al. 2008; Bally et al. 2010)

$$M = \frac{D^2\, S_\nu\, R_t}{B_\nu(T_\mathrm{d})\, \kappa_\nu}, \tag{1}$$

where D is the distance, S_ν is the integrated flux density, R_t is the gas-to-dust mass ratio (taken as 100), $B_\nu(T_\mathrm{d})$ is the Planck function at dust temperature T_d (taken as 10 K), and κ_ν is the dust opacity (1.14 cm^2 g^{-1}) (Enoch et al. 2006; Dewangan et al. 2016). The above equation assumes that the emission (at 1.1 mm here) is optically thin, and both T_d and $\kappa_{1.1\,\mathrm{mm}}$ are position independent within a core. Using the retrieved integrated flux densities of ~8.316 and 1.300 Jy for the central and southwestern clumps, respectively, the resultant masses were calculated to be ~10,274 and 1606 $M_\odot$, respectively. The southwestern Bolocam clump is also associated with a *hub*, as is evident in Figure 2 from the column density contour (solid magenta contour within the cyan box). We find that while the

[8] https://irsa.ipac.caltech.edu/

southwestern Bolocam clump has a mass of the order of magnitude similar to other hubs from literature (i.e., $\sim 10^3\,M_\odot$), such as Mon R2 (Treviño-Morales et al. 2019; Kumar et al. 2022), SDC13 (Williams et al. 2018), and others (Hacar et al. 2022), the mass for the central Bolocam clump is an order of magnitude larger. This is probably due to the fact that the integrated flux density covers a wider emission region (Rosolowsky et al. 2010) than the mere hub. If one were to use the flux density within an 80″ diameter aperture for the central clump (an area roughly coincident with the $N(H_2) \sim 10^{22}\,cm^{-2}$ hub region)—also given in the catalog (∼3.814 Jy)—a mass of $\sim 4712\,M_\odot$ is obtained, which is of the order of magnitude as for other studies in the literature.

3.2. Molecular Gas Kinematics in the Central Region

We now examine the central part of the Sh2-138 region (see the field of view marked in Figure 1 (right)) using (spatial and spectral) higher-resolution CO(3–2), ^{13}CO(3–2), and C^{18}O(3–2) molecular line data retrieved from the JCMT archive. The field of view of each cube is $\sim 5' \times 5'$ and roughly encloses the hub and central core of CGPS CO emission. For ^{13}CO and C^{18}O, the rebinned cubes with 0.5 km s^{-1} channel width have been used to examine the spatial structures in the following sections as their lower noise (see Section 2) allows for better examination of features. However, for the calculation of physical parameters (in Section 3.2.4), the native channel width (∼0.05 km s^{-1}) ^{13}CO and C^{18}O cubes have been utilized as we need high-velocity resolution here.

Figure 5 shows the channel maps of the ^{13}CO(3–2) emission. The velocity range for each frame has been given. In the [−50, −49] km s^{-1} velocity range, two prominent filamentary structures can be traced, and these have been indicated by arrows. The filament along the southwest direction (SW-f) is longer and much more prominent. It can only be seen in the −51 to −49 km s^{-1} velocity range, and has no counterparts at larger or smaller velocities. The second filament, pointing west (W-f), is also seen prominently in the −51 to −49 km s^{-1} velocity range but can be traced as diffused emission at larger and smaller velocities. As we move toward higher (absolute) velocities, a third filament can be traced in the −56 to −51 km s^{-1} range in the southeast direction (SE-f), and is most prominently seen in the [−53, −52] km s^{-1} channel map. Apart from the filaments, another prominent feature is the sudden depression in emission—along the southeast to northwest axis—seen in the [−53, −52] and [−52, −51] km s^{-1} channel maps. At larger and smaller velocity channel maps, this depression shows the presence of diffuse emission. It should be noted that the systemic velocity of the cloud complex is $\sim -51.7 \pm 1.9$ km s^{-1}(see Section 3.2.4). We note that the abovementioned features (filaments and depression) could also be traced in the C^{18}O(3–2) channels, albeit not at the requisite signal-to-noise threshold (see Section 3.2.1).

3.2.1. Moment Maps

To account for the noise in the cubes, we confine our further analysis to only those regions with detections above 5σ (where σ is the data's rms noise level). Using the clumpfind algorithm (Williams et al. 1994) as implemented in the CUPID package (Berry et al. 2007) of the STARLINK software suite (Currie et al. 2014), clumps were identified in the position–position–velocity spectral cube. The threshold for detection was kept conservatively at 5σ to avoid the possibility of false detections, and the gap between contour levels at 2σ as is recommended by Williams et al. (1994). The clumps detected in all three spectral cubes (CO(3–2), ^{13}CO(3–2), and C^{18}O(3–2)) lay in the range (−60, −45) km s^{-1}. Thereafter, the regions with non-detection were masked to construct masked cubes for all three molecular lines.

Figure 6 shows the moment-0 (integrated emission), moment-1 (intensity-weighted velocity), and line width (intensity-weighted dispersion) collapsed images from all three (masked) cubes. In the intensity-weighted velocity map for CO(3–2), high-velocity gas is interspersed with low-velocity gas throughout and no particular pattern is discernible. For ^{13}CO(3–2), as in the case of integrated intensity emission, filamentary structure is noticeable here as well. The SW-f filament (see Figure 5) shows a lower (absolute) velocity than other parts of the region. Such a velocity profile would suggest a gradient (at the joint between the SW-f filament and the central part) resulting in gas flow. To better understand the same, position–velocity slices were taken along the two vector directions (east–west and north–south) marked on this image, which we elaborate upon in Section 3.2.2.

The intensity-weighted dispersion maps are shown in the last row of this image grid. The central part of the cloud shows a large velocity dispersion, of the order of about 2 km s^{-1} in all three molecular lines, yet another indication of mixing of flows. This large dispersion is seen to extend along the northeast part of the image in both CO(3–2) and ^{13}CO(3–2) molecular lines. In contrast, the southwest filament (traced prominently in ^{13}CO(3–2)) shows a relatively smaller dispersion of ∼1 km s^{-1}. CO(3–2) is the most ubiquitous tracer of molecular hydrogen and shows diffused emission in the entire region in the integrated intensity map. ^{13}CO(3–2) has a higher critical density and thus shows the filamentary nature prominently, while C^{18}O(3–2), which has the highest critical density, primarily traces the central clump.

3.2.2. Position–Velocity Slices

Figure 7 shows the position–velocity maps along the two directions marked in the ^{13}CO(3–2) intensity-weighted velocity map in Figure 6(e). The first figure shows the slice for the east–west vector and the second figure shows the slice for the north–south vector. Along both the slices, there appears to be a significant velocity gradient as one moves along the vector. Vertical dotted lines mark the intervals between which an appreciable gradient can be seen. The east–west slice shows the absolute velocity increasing from ∼52 to 54 km s^{-1}, then decreasing to below 51 km s^{-1} and then again increasing to above 52 km s^{-1}. A similar pattern is observed in the north–south slice, where the velocity first increases slightly and then decreases as one moves along the vector, i.e., from offset 0° to 0°.06 (∼6 pc). In Figure 7 (left), the offset from ∼0°.044 onward is roughly coincident with the W-f filament, and in Figure 7(right), the offset from ∼0°.032 to 0°.052 represents the SW-f (see ^{13}CO(3–2) moment-1 map in Figure 6(e)). As was also seen in the moment-1 map, the velocity is nearly constant at ∼−52 km s^{-1} and −51 km s^{-1} along the W-f and SW-f filaments, respectively. A small gradient is seen only toward

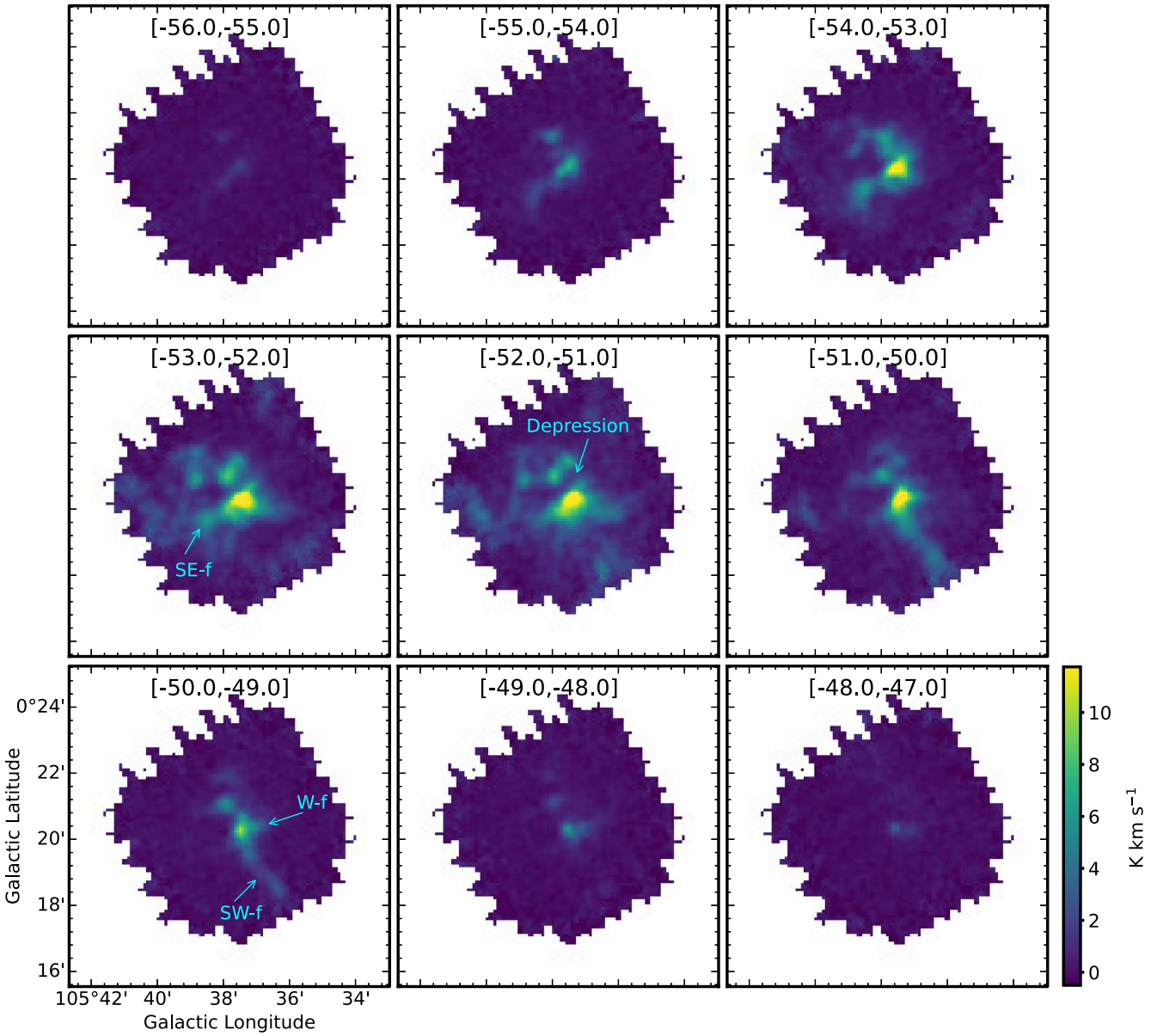

Figure 5. Channel maps of ^{13}CO(3–2) emission. Three filamentary structures: W-f, SW-f, and SE-f can be traced on the images. A region of minima in emission has been marked as "Depression" in the [−52, −51] km s^{-1} channel map.

the end for the SW-f filament. This gradient coincides with the position of peak(s)/clump(s) (discussed below in Section 3.2.3) and could thus denote gas being channeled into the clump. Overall, this gradient pattern in both slices is indicative of gas spiraling into the central region from both ends of the molecular cloud. There also appears to be clumping of gas, with the brightest clump (roughly at an offset of 0.°032 and 0.°02 in Figures 7 (left) and 7 (right) respectively) being that of the central region. Another noticeable feature in the north–south slice (Figure 7 (right)) is the presence of a dark region at an offset of ∼0.°012 in the velocity range of −52 to −51 km s^{-1}. There is only a faint connecting feature between the immediate northern and southern clumps at ∼−54 to −53 km s^{-1}. This dark region corresponds to the prominent gap seen in the channel map (marked "Depression" in the [−52, −51] km s^{-1} channel map in Figure 5). In the central region, we find material clumping at two distinct velocities of –51 and −53 km s^{-1}. Overall, the maps show considerable dispersion in the velocity space around the systemic velocity of the cloud complex (∼−51.7 km s^{-1}), possibly due to the two directions being along the two outflow axes in the region (see Section 4 for further discussion).

3.2.3. Analysis of ^{13}CO(3–2) and Herschel Clumps

Figure 8 shows the ^{13}CO(3–2) integrated emission along with the Herschel 250 μm map of the region. Contours have been drawn on both images for better clarity of the features. Boxes on both images mark the locations where spectra have been extracted. Since the beam size is of the order of ∼2 pixels, spectra were extracted for a 2 × 2 box encompassing the pixel with the local maxima. Red boxes mark the regions that show a (local) peak in the ^{13}CO(3–2) integrated intensity map, while magenta boxes (c3, c4, c10, c13, c16) mark the locations of those peaks that are seen in the 250 μm image but not traced clearly in the integrated intensity image. Blue boxes mark the locations that do not display any peak, but are along the filaments that can be

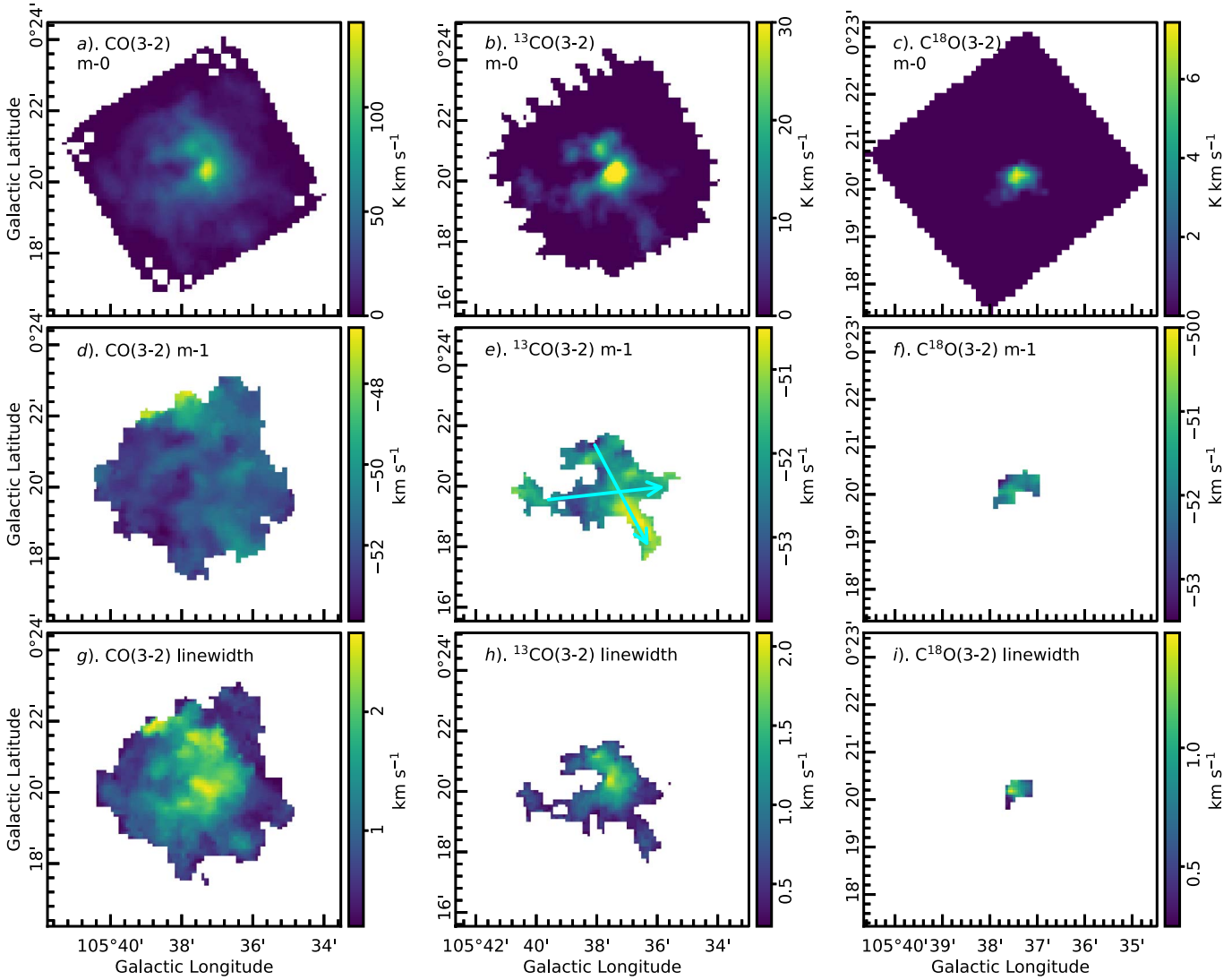

Figure 6. Row-wise: moment-0 (integrated intensity), moment-1 (intensity-weighted velocity), and line width (intensity-weighted dispersion) collapsed images for three cubes—CO(3–2), ^{13}CO(3–2), C^{18}O(3–2)—in the first, second, and third columns, respectively. Cyan vectors in the ^{13}CO(3–2) moment-1 map mark the directions along which position–velocity slices have been extracted.

delineated, –c6 and c7 for the W-f filament shown in Figure 5, c8 and c9 for the SW-f filament shown in Figure 5. The ^{13}CO(3–2) molecular line spectra extracted at these locations are shown in Figure 9. For the central clump, marked c5, C^{18}O(3–2) emission was also detected at above 5σ threshold, and hence C^{18}O(3–2) molecular line spectrum has also been plotted for this location in Figure 9 (weaker step-line plot in the frame for c5). It should be noted that the massive stars studied by Deharveng et al. (1999) and Baug et al. (2015) are associated with the location of c5.

An obvious feature to note here is that the locations c2, c4, and c5 show self-absorption near the peaks. While the spectrum for c5 (the central clump) is nearly symmetrical around the self-absorption *dip* in the spectrum, those for c2 and c4 are asymmetrical. The location c4 particularly seems to be having high self-absorption, indicative of dense material present in this part. It is worth noting that while the c4 clump is prominently observed in the thermal dust emission wavelength at 250 μm, the location shows a depression in ^{13}CO(3–2) molecular line emission. This can be seen in the integrated emission in Figure 8 (left) as well as in the channel maps in Figure 5. c4 lies in the prominent gap marked in the $[-52, -51]$ km s^{-1} channel map shown in Figure 5. It is also almost coincident with the gap seen in the position–velocity slice (see Figure 7 (right) at around an offset of 0.°012) along the north–south vector (see intensity-weighted velocity map of ^{13}CO(3–2) in Figure 6(e)). We note that the weaker velocity component from the CGPS CO(1–0) spectra (see Figure 3) is barely seen and only for a few peaks (such as c8, c13, c14, c17, and c18) due to the weak nature of this emission. The low number of pixels used to extract spectra at these locations makes this component virtually indistinguishable from the noise. An averaged spectrum over the entire JCMT field of view does indeed reveal this component (not shown here).

3.2.4. Physical Parameters

To extract the parameters for further calculations, we carried out Gaussian model fitting for each region in the velocity range $[-60, -45]$ km s^{-1} on the (non-averaged) ^{13}CO and C^{18}O spectral cubes with a native channel width of $\sim$0.05 km s^{-1}. The Gaussian fits to the ^{13}CO(3–2) molecular line emission are shown with a green line in all the spectra (Figure 9). The results of the model fitting of the clumps, along with other parameters,

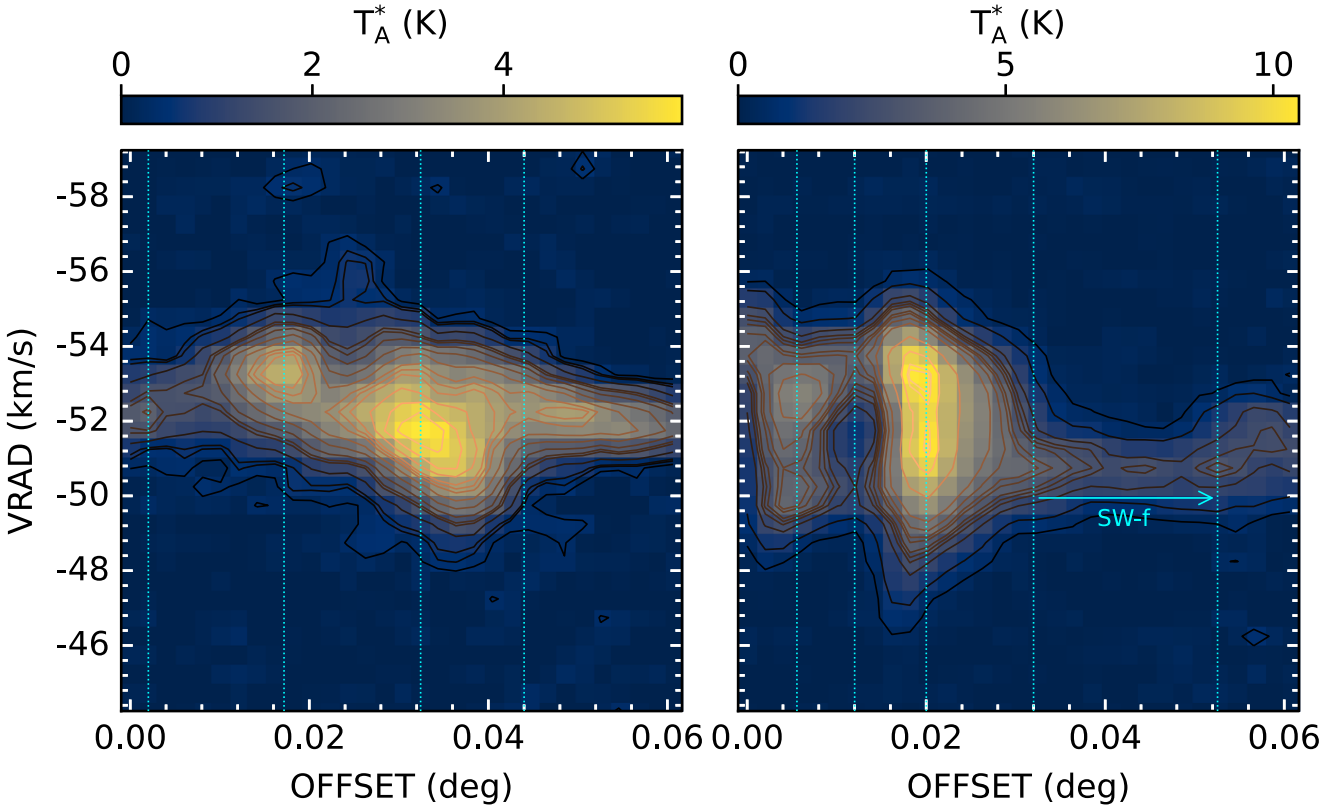

Figure 7. Position–velocity maps along the two vector directions marked in the ^{13}CO(3–2) intensity-weighted velocity map in Figure 6(e). Left: along the east–west vector (contours at 0.3, 0.5, 0.6, 1, 1.5, 1.65, 2, 2.5, 3, 3.5, 3.75, 4, 4.5, 5, 5.5, and 6 K). Right: along the north–south vector (contours at 0.45, 1, 2, 2.5, 2.75, 3, 3.5, 3.75, 4.25, 5, 7, 9, 10, and 10.25 K). Vertical dotted lines mark the intervals between which an appreciable gradient can be seen. SW-f is the filament shown in Figure 5.

are listed in Table 2. As mentioned earlier, for the c5 central clump, C^{18}O(3–2) spectrum was also available, and has been shown as well along with its Gaussian fit. Both isotopologues were found to have similar peak velocities, $\sim -51.7 \pm 1.9$ and -52 ± 2 km s^{-1} for C^{18}O and ^{13}CO, respectively. Since C^{18}O traces the densest part of the cloud, its velocity can be taken as the systemic velocity of the cloud complex, and is in agreement with the literature (Blitz et al. 1982; Burov et al. 1988; Harju et al. 1993; Johansson et al. 1994; Bronfman et al. 1996).

The Gaussian model fit was used to obtain the FWHM and standard deviation (or velocity dispersion) for each region. Thereafter, we calculate the nonthermal velocity dispersion and total velocity dispersion using the following equations (Fuller & Myers 1992; Fiege & Pudritz 2000):

$$\Delta V_{\rm tot}^2 = \Delta V_{\rm obs}^2 + 8 \ln 2 \, kT \left(\frac{1}{\bar{m}} - \frac{1}{m_{\rm obs}} \right)$$

$$\Rightarrow \frac{\Delta V_{\rm tot}^2}{8 \ln 2} = \frac{kT}{\bar{m}} + \left(\frac{\Delta V_{\rm obs}^2}{8 \ln 2} - \frac{kT}{m_{\rm obs}} \right), \quad (2)$$

$$\Rightarrow \sigma_{\rm tot}^2 = c_s^2 + (\sigma_{\rm obs}^2 - \sigma_{\rm T}^2), \quad (3)$$

$$= c_s^2 + \sigma_{\rm NT}^2, \quad (4)$$

where $\Delta V_{\rm obs}$ and $\sigma_{\rm obs}$ ($=\Delta V_{\rm obs}/\sqrt{8 \ln 2}$ for a Gaussian) are the FWHM and standard deviation (or dispersion), respectively, from the observed spectrum of the molecular species; $\sigma_{\rm T} (=\sqrt{kT/m_{\rm obs}})$ is the thermal velocity dispersion for the molecular species; $m_{\rm obs}$ is the mass of the molecule (29 and 30 amu for ^{13}CO and C^{18}O, respectively); $\sigma_{\rm NT}$ is the nonthermal velocity dispersion; $c_s (=\sqrt{kT/\bar{m}})$ is the speed of sound; $\bar{m}$ is the average molecular weight of the medium (2.37 amu); and T is the excitation or gas kinetic temperature.

The critical density for ^{13}CO(3–2) is in the range of $\sim 10^{4\text{-}5}$ cm^{-3}, and if we assume the gas and dust temperatures to be coupled via collisions at this density (Goldsmith 2001), then the dust temperature from the Herschel ViaLactea temperature map can be used for gas kinetic temperature T in the above equation. We add a caveat though that, depending on the physical conditions of the region, a significant difference between the gas and dust temperatures can still exist (Banerjee et al. 2006; Koumpia et al. 2015). The median temperature at the locations of the peaks ranged from 18–20 K ($c_s \sim$ 0.25–0.27 km s^{-1}), with the c4 and c5 clumps at 28 K ($c_s \sim 0.31$ km s^{-1}). At these temperatures, the thermal velocity dispersion $\sigma_{\rm T}$ (for both ^{13}CO and C^{18}O) is calculated as $\sim$0.07–0.09 km s^{-1}. Table 2 lists these calculated values for the clumps associated with the peaks in Figure 8.

The FWHM values for almost all the peaks lie in the $\sim$2–2.75 km s^{-1} range (and thus $\sigma_{\rm obs} \sim 0.85$–1.2 km s^{-1}), except for c2, c4, and c5 which lie in $\sim$4–4.7 km s^{-1} range ($\sigma_{\rm obs} \sim 1.7$–2 km s^{-1}). This was also observed in the line width map in Figure 6(h). For c13, the lower value might be due to the noisy spectrum. As $\sigma_{\rm obs}$ is much larger than $\sigma_{\rm T}$ (0.07–0.09 km s^{-1}) for all the cases, we find it to be almost the same as $\sigma_{\rm NT}$. The c2, c4, and c5 locations have the highest nonthermal dispersions. Using the above variables, we subsequently calculated the Mach number ($=\sigma_{\rm NT}/c_s$) and the ratio of thermal-to-nonthermal pressure ($P_{\rm TNT} = c_s^2/\sigma_{\rm NT}^2$) as well (Lada et al. 2003). All the locations were found to have

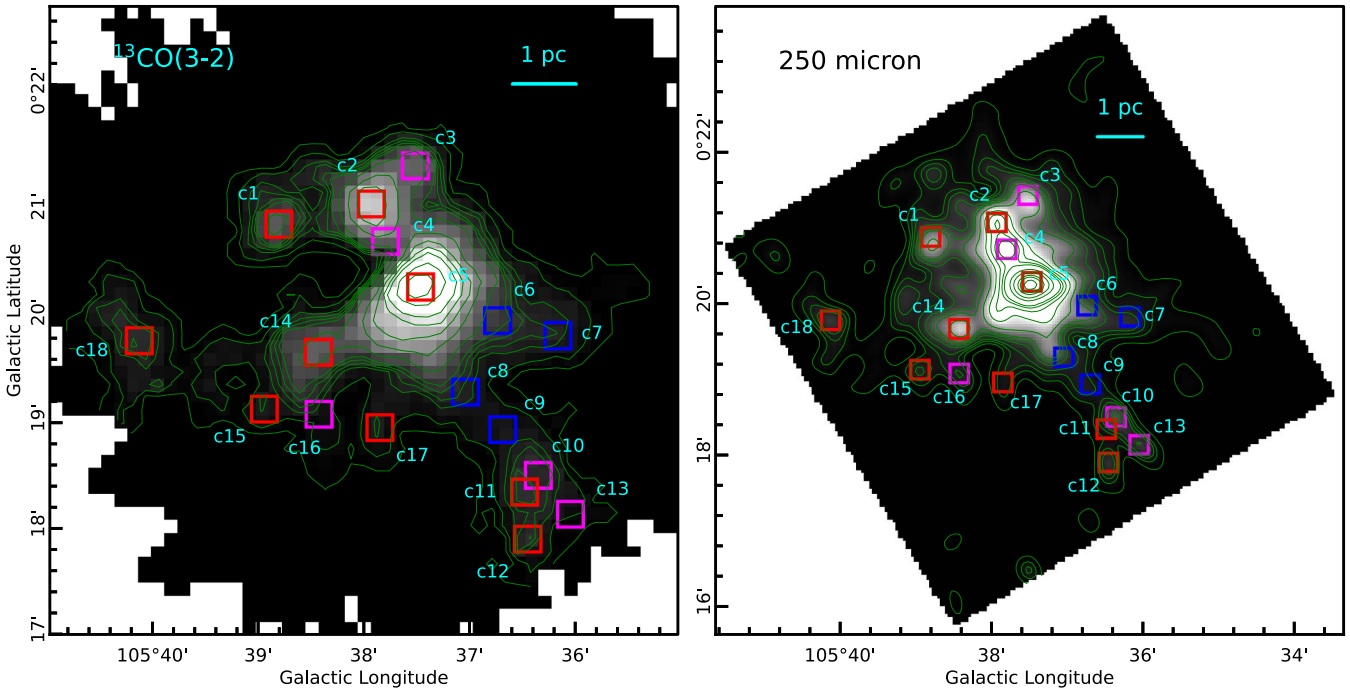

Figure 8. Left: ^{13}CO(3–2) integrated intensity map (contours at 0.45, 2, 4, 5, 6, 7, 10, 15, 20, 25, 30, 40, and 50 K km s^{-1}). Right: Herschel 250 μm image (contours at 0.23, 0.3, 0.35, 0.4, 0.5, 0.6, 0.7, 1, 1.5, 2, 2.5, 3, 5, 7, 10, 12, and 15 $\times$ 10^3 MJy sr^{-1}). Red boxes mark the peaks seen in the integrated intensity map, while magenta boxes mark those that are primarily seen in the 250 μm image (and are not noticeable in the first image). Blue boxes mark the locations that do not display any peaks, but where spectra for the W-f and SW-f filaments (Figure 5) were extracted.

Mach numbers, which suggest supersonic motion, with c2 and c5 displaying the largest values ($\gtrsim$6). The order of magnitude of $P_{\rm TNT}$ ($\sim$0.01–0.1) indicates that nonthermal pressure dominates in the cloud, and the locations of highest nonthermal dispersion and Mach numbers (i.e., c2, c4, and c5) were found to be correlated to the least ratio values.

Myers (2009) posits a hub-filament model of star-forming complexes where the hub (Kumar et al. 2020) is traced at a high column density of $\sim$10^{22} cm^{-2} as opposed to the filaments (André 2015; Arzoumanian et al. 2013), which have a column density of $\sim$10^{21} cm^{-2}. For the three filaments, SW-f, W-f, and SE-f (see Figure 5), we calculated the line mass using the Herschel column density map constructed from thermal dust emission (see Section 2). The length of the three filaments was taken from the 10^{22} cm^{-2} contour (i.e., the inner extent) along the line joining c6 and c7 for the W-f filament; c8, c9, and c10 for the SW-f filament; and up to c14 for the SE-f filament. The total column density was summed up in a width of 12″ (corresponding to $\sim$0.33 pc at a distance of 5.7 kpc) as it is the resolution of the column density map. Thereafter, using the following formula (Mallick et al. 2015; Dewangan et al. 2017b):

$$M_{\rm line,obs} = \frac{\mu_{\rm H_2}\, m_{\rm H} {\rm area}_{\rm pixel}\, \Sigma N({\rm H_2})}{({\rm length\ of\ filament})}, \quad (5)$$

where $\mu_{\rm H_2}$ is the mean molecular weight (2.8), $m_{\rm H}$ is the mass of hydrogen, ${\rm area}_{\rm pixel}$ is the area subtended by one pixel, and $\Sigma N({\rm H_2})$ is the total column density—we calculated the (observed) line masses to be $\sim$ 32, 33.5, and 50 $M_\odot$ pc^{-1} for the filaments W-f, SW-f, and SE-f, respectively.

4. Discussion

According to the multiwavelength study of Baug et al. (2015), Sh2-138 represents the archetype *hub-filament* structure of Myers (2009), which—after the advent of Herschel far-infrared data—has been found to be a ubiquitous feature of young stellar clusters hosting low-mass and high-mass stars (Kumar et al. 2020). However, this interpretation needs to be tempered by the fact that most of the filamentary clouds whose intricate structure has been studied in the literature have been nearby regions such as Monoceros R2 (Treviño-Morales et al. 2019, 830 pc), W40 (Mallick et al. 2013, 500 pc), IC 5146 (Arzoumanian et al. 2011, 460 pc), and others (Arzoumanian et al. 2019; Hacar et al. 2022). Though regions at further distances have been explored in the literature, such as IRAS 05480+2545 (Dewangan et al. 2017a, 2.1 kpc), Sh2-53 (Baug et al. 2018, 4 kpc), G18.880.49 (Dewangan et al. 2020, 5 kpc), and so on, the larger distance often makes it difficult to resolve finer structures. The large-scale view of the Sh2-138 region shows filaments whose sizes are of the order of $\sim$10 pc. Such large filaments (at distances of a few kiloparsecs) have also been discussed in various studies—with the Nessie cloud often held up as an archetype, and terminologies such as *giant molecular filaments* and *Milky Way bone* having been employed for such large filaments (Ragan et al. 2014; Zucker et al. 2018). Nevertheless, as also discussed in Kumar et al. (2020), it is possible that higher-resolution studies of distant regions could resolve a large filament into structures with size scales similar to those of the nearby regions. The higher-resolution JCMT and Herschel maps for the central region seem to suggest this where we can see more detailed structures. The filamentary structures in the central region have sizes of the order of a few parsecs, which is not so uncommon. Examples of some of the massive star-forming regions from the

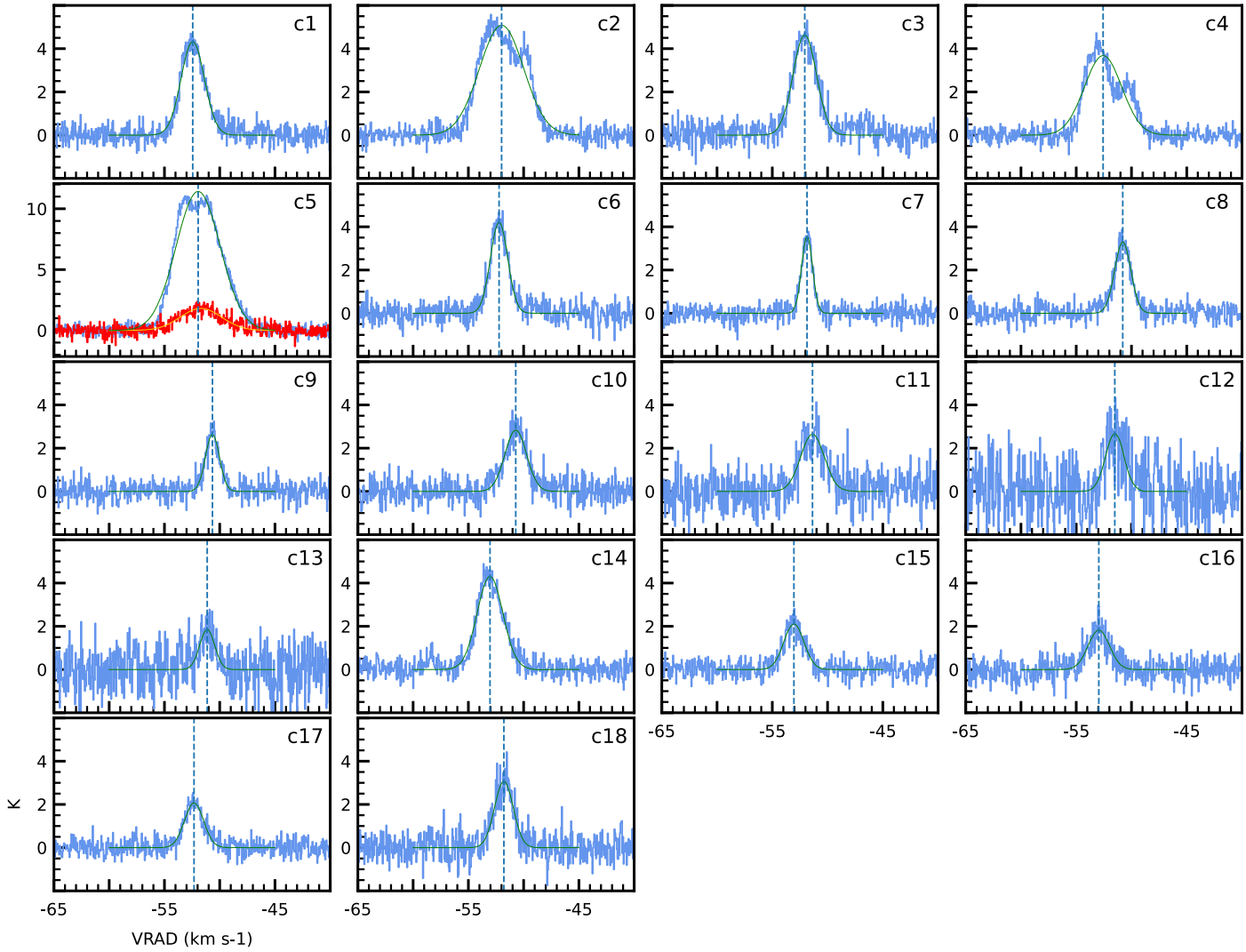

Figure 9. ^{13}CO(3–2) spectra at positions marked in Figure 8. The green curve denotes the Gaussian fit to the spectra, with the blue dashed line marking the velocity of the peak of the Gaussian fit. For c5, C^{18}O(3–2) the spectrum is plotted in red and the Gaussian model fit is shown by the yellow curve.

literature where such length scales have been observed are G22 (Yuan et al. 2018, 3.51 kpc), DR21 (Hennemann et al. 2012, 1.4 kpc), and SDC13 (Peretto et al. 2014, 3.6 kpc), though the line masses for these regions are larger with a wide range, varying from ∼2 up to 20 times our line masses. On the other hand, nearby regions such as IC 5146 (Arzoumanian et al. 2011, 460 pc) show a wide span of line masses for filaments of lengths of a few parsecs, from ∼ 0.5–3 times our line masses.

Hacar et al. (2022) used a census of more than 22,000 filaments from the literature to categorize them into different (non-mutually exclusive) families. A comparison of the structure and physical parameters of the filamentary structures in Sh2-138 with their compilation shows that while our filaments are similar to the *dense fiber* filament family in their categorization in terms of being structures in position–position–velocity space, our filaments display a larger nonthermal dispersion (σ_{NT}). Higher σ_{NT} values are seen for *Galactic plane survey filaments* and *giant filaments* (see Table 2 of Hacar et al. 2022). As discussed for these two filament families in Hacar et al. (2022), the calculation of physical parameters could suffer from sensitivity and resolution biases, given the 5.7 kpc distance for the region, as well as be affected by the tracer used for calculations. High values of σ_{NT} and Mach number have been determined to be a result of large-scale accretion flows resulting in internal turbulence, and when filament networks (with disparate velocity centroids) are observed with low-resolution beams, the resulting measurements of line width are expected to be supersonic (Hacar et al. 2016).

The central part of the Sh2-138 region has been mapped by the JCMT CO(3–2), ^{13}CO(3–2), and C^{18}O(3–2) molecular lines. These molecular lines trace the warm and dense gas in the temperature range of 10–50 K and density $\sim 10^{4-5}$ cm^{-3}, enveloping the cores where star formation is taking place (Davis et al. 2010). Three main filaments—labeled W-f, SW-f, and SE-f –can be traced on the ^{13}CO(3–2) channel map (Figure 5). While one end of the SW-f and SE-f filaments merges into the hub, the morphology at the other ends of these two filamentary structures shows other possible filaments branching from them. For example, in Figure 8, the SW-f ("c8-c9-c10") filament seems to be branching into "c10-c11-c12" and "c10-c13"; and the SE-f filament seems to be branching into "c14-c15" and "c14-c16." It is possible that they represent secondary filaments that merge into a primary filament (SW-f and SE-f here), which then merges into the hub. Such structure has been seen for regions like Monoceros R2 (Treviño-Morales

Table 2
Parameters Derived from ^{13}CO(3–2) Spectra at the Locations of Peaks Shown in Figure 8

Clump	FWHM (km s^{-1})	T (K)	σ_{NT} (km s^{-1})	Mach Number	P_{TNT}
c1	2.48	20	1.05	3.97	0.06
c2	4.71	20	2.00	7.55	0.02
c3	2.50	20	1.06	3.99	0.06
c4	3.98	28	1.69	5.39	0.03
c5					
C^{18}O	4.39	28	1.86	5.95	0.03
^{13}CO	4.69	28	1.99	6.35	0.03
c10	2.30	18	0.98	3.88	0.07
c11	2.53	18	1.07	4.26	0.05
c12	1.97	18	0.83	3.31	0.09
c13	1.60	18	0.68	2.69	0.14
c14	2.75	20	1.17	4.40	0.05
c15	2.14	18	0.91	3.61	0.08
c16	2.27	18	0.96	3.83	0.07
c17	2.03	18	0.86	3.42	0.09
c18	1.99	18	0.84	3.35	0.09

Note. For c5, C^{18}O(3–2) spectrum was also available and thus used for calculation as well.

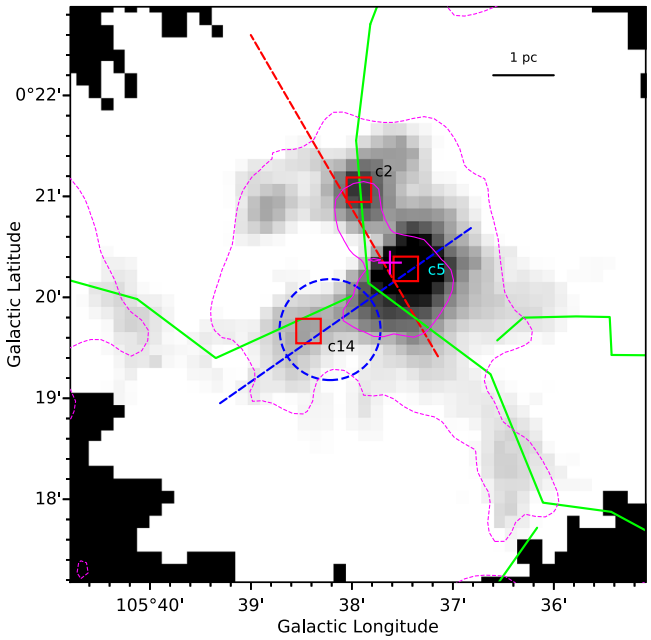

Figure 10. JCMT ^{13}CO(3–2) integrated intensity map. Magenta dashed and solid contours mark $N(H_2) = 33 \times 10^{20}$ cm^{-2} and 10^{22} cm^{-2}, respectively, from the ViaLactea maps. Dashed blue and red lines mark the major axes of blue and red outflow contours, respectively, from Qin et al. (2008). The magenta plus symbol shows the location of IRAS 22308+5812. The green lines represent the filament skeletons shown in Figure 2. The clumps c2, c5, and c14 shown in Figure 8 are marked by red boxes and labeled.

et al. 2019; Kumar et al. 2022). Furthermore, at the end of the SW-f filament shown in Figure 7 (right), a clump is seen at an offset of ∼0.°052 (marked with a dashed vertical line). This clump corresponds to ∼c10-c11 in Figure 8, which seems to be accreting matter from further along the filament length, given the small gradient that is seen in the 0.°052–0.°06 offset range in Figure 7 (right). Along the length of the W-f and SW-f filaments marked in the position–velocity diagrams in Figures 7 (left) and (right), respectively, clumping of gas can also be seen. The position–velocity maps (Figure 7) show a velocity gradient as one approaches the central clump region, which indicates gas being channeled from outer regions to the central region. The relatively large velocity dispersion in the central part of the cloud in all three isotopologues (Figure 6) is indicative of this. The scenario that emerges is that of longitudinal flow along filaments converging on a stellar cluster (Peretto et al. 2014; Treviño-Morales et al. 2019; Kumar et al. 2020).

Figure 10 shows the JCMT ^{13}CO(3–2) integrated intensity map with overlaid column density contours, outflow axes, and the *getsf* filamentary skeletons from Figure 2 within this field of view. The peak of the blueshifted outflow emission has been indicated by a dashed blue circle and it coincides with the peak c14 shown in Figure 8. The trapezium-like cluster from Deharveng et al. (1999) (including am Herbig Be star; Baug et al. 2015) is coincident with the IRAS source marked here, which is far away from the blue lobe peak is unlikely to be the driving source of the blue outflow lobe. The cluster of young stellar objects (in which some are of intermediate mass) identified by Baug et al. (2015) that lie within the area of the blue lobe peak could be partially driving the outflow, or alternatively, c14 could be a source in the initial stages of star formation. As such, this source could be a suitable candidate as a subject of a detailed investigation. Comparing Figures 6 and 10, one can see that the northern (eastern) part of the north–south (east–west) vector in Figure 6(e) is almost coincident with the red (blue) lobe axis in Figure 10. Thus the complex structure in the position–velocity diagram shown in Figure 7 (right) (∼offset 0.°00–0.°02, corresponding to the northern part of the north–south vector shown in Figure 6(e)) could be a combination of the turbulence injected along the directions by the outflow and/or phenomena such as Hubble flow (Arce & Goodman 2001; Ridge & Moore 2001), mass entrainment, and so on (Lada & Fich 1996; Arce & Goodman 2002). Zinchenko et al. (2020) in their study of S255IR high-mass star-forming region observed that walls around outflow cavities could appear as filaments in projection. Given the arrangement of *getsf* filaments and outflow axes for the Sh2-138 region (Figure 10), such a situation is also a possibility here and merits further investigation of the region in different molecular species. It is also worth noting that the central hub region (magenta solid contour in Figure 10) seems to have two centers (c2 and c5), also seen in other regions such as NGC 2264 (Kumar et al. 2020) and G31.41+0.31 (Beltrán et al. 2022).

Looking at the combined large-scale field of view (Section 3.1) and the central portion (Section 3.2) from the context of star formation frameworks, one finds that there could be the applicability of scenarios such as the global hierarchical collapse (Vázquez-Semadeni et al. 2019), the *conveyor belt* model (Longmore et al. 2014; Krumholz & McKee 2020), and the HFS model (Kumar et al. 2020) based on the longitudinal flows. There also appears to be isolated star formation all along the filament F1 shown in Figure 4, and though the isolated 1.1 mm emission clump seems to be associated with a hub (based on the column density), it does not appear to be lying at any junction of filaments. A caveat, however, could be that merging filaments at this clump is directed nearly orthogonal to the plane of the sky in the line of sight. Finally, we note that there are studies in the literature that—based on molecular line spectra—have suggested the existence of multiple clouds in

various regions and subsequent *cloud–cloud collision*, wherein collision between molecular clouds leads to a shock-compressed layer with density enhancement, due to which filament formation as well as high-mass star formation can occur (Scoville et al. 1986; Habe & Ohta 1992; Tan 2000; Anathpindika 2010; Inoue & Fukui 2013; Takahira et al. 2014; Fukui et al. 2021). Though multiple peaks in the CO spectra are seen for this region too (Section 3.1), such a scenario however, is tough to conclude and would require observations in molecules that trace the dense gas of shock-compressed layers, such as NH_3 and HCN (Priestley & Whitworth 2021) to justify.

5. Summary and Conclusions

In this paper, we have carried out a molecular line study of the HFS in the Sh2-138 region. The primary data utilized was CO(1–0) transition from CGPS for the wider $\sim 50' \times 50'$ region, and the CO(3–2), ^{13}CO(3–2), and C^{18}O(3–2) transitions from the JCMT archive for the central $\sim 5' \times 5'$ region. Our main conclusions are as follows:

1. CGPS CO(1–0) integrated intensity emission of the region shows it to be an HFS of approximately a few tens of parsecs in scale. The central region shows a spectrum with two velocity components. The axes of outflows in the region from the literature were found to be aligned along the filaments detected via the *getsf* tool.
2. In the large-scale field of view, one of the filaments (labeled "F1" in our analysis) appears to be a site of active star formation. It is associated with diffused ionized emission at a junction with another filament (labeled "F2") and was found to be hosting a 1.1 mm emission clump of mass $\sim 1606\, M_{\odot}$.
3. Analysis of the central $\sim 5' \times 5'$ area in ^{13}CO(3–2) emission found three filamentary structures—labeled W-f, SW-f, and SE-f—above a 5σ detection threshold. The observed line mass ($M_{\rm line,obs}$) was calculated to be $\sim$50, 32, and 33.5 $M_{\odot}$ pc^{-1} for SE-f, W-f, and SW-f, respectively.
4. The clump labeled c14, detected in Herschel 250 μm emission as well as ^{13}CO(3–2) integrated intensity emission (at $>5\sigma$) was found to coincide with the peak emission region of the blue outflow lobe, and merits future investigation as a protostellar candidate.
5. Position–velocity slices (east–west and north–south slice) across the filaments revealed velocity gradients that point toward longitudinal flow along the filaments converging onto the central dense clump.
6. A Gaussian model fitting of the spectra at different locations showed a dominance of nonthermal motion—with a large nonthermal dispersion and a small value of the ratio of thermal-to-nonthermal pressure ($\sim$0.01–0.1). Mach number ($\gtrsim$3) analysis indicates the presence of large supersonic motions within the clumps.

We thank the anonymous referee for the critical reading of the manuscript and the suggestions that improved this paper. D.K.O. acknowledges the support of the Department of Atomic Energy, Government of India, under project Identification No. RTI 4002. I.I.Z. acknowledges support from the IAP RAS program FFUF-2021-0005. The research work at the Physical Research Laboratory is funded by the Department of Space, Government of India. T.B. acknowledges the support from the S.N. Bose National Center for Basic Sciences under the Department of Science and Technology (DST), Government of India. The Canadian Galactic Plane Survey (CGPS) is a Canadian project with international partners. The Dominion Radio Astrophysical Observatory is operated as a national facility by the National Research Council of Canada. The Five College Radio Astronomy Observatory CO Survey of the Outer galaxy was supported by NSF grant AST 94-20159. The CGPS is supported by a grant from the Natural Sciences and Engineering Research Council of Canada. JCMT has historically been operated by the Joint Astronomy Center on behalf of the Science and Technology Facilities Council of the United Kingdom, the National Research Council of Canada, and the Netherlands Organization for Scientific Research. This research has made use of the NASA/IPAC Infrared Science Archive, which is funded by the National Aeronautics and Space Administration and operated by the California Institute of Technology.

Facilities: JCMT, Herschel, IRSA.

ORCID iDs

Kshitiz K. Mallick https://orcid.org/0000-0002-3873-6449
Lokesh K. Dewangan https://orcid.org/0000-0001-6725-0483
Devendra K. Ojha https://orcid.org/0000-0001-9312-3816
Tapas Baug https://orcid.org/0000-0003-0295-6586
Igor I. Zinchenko https://orcid.org/0000-0003-2793-8229

References

Aguirre, J. E., Ginsburg, A. G., Dunham, M. K., et al. 2011, ApJS, 192, 4
Anathpindika, S. V. 2010, MNRAS, 405, 1431
Anderson, L. D., Bania, T. M., Balser, D. S., et al. 2014, ApJS, 212, 1
André, P. 2015, HiA, 16, 31
Arce, H. G., & Goodman, A. A. 2001, ApJ, 554, 132
Arce, H. G., & Goodman, A. A. 2002, ApJ, 575, 911
Arzoumanian, D. 2017, arXiv:1712.00604
Arzoumanian, D., André, P., Didelon, P., et al. 2011, A&A, 529, L6
Arzoumanian, D., André, P., Könyves, V., et al. 2019, A&A, 621, A42
Arzoumanian, D., André, P., Peretto, N., & Könyves, V. 2013, A&A, 553, A119
Bally, J., Aguirre, J., Battersby, C., et al. 2010, ApJ, 721, 137
Banerjee, R., Pudritz, R. E., & Anderson, D. W. 2006, MNRAS, 373, 1091
Baug, T., Dewangan, L. K., Ojha, D. K., et al. 2018, ApJ, 852, 119
Baug, T., Ojha, D. K., Dewangan, L. K., et al. 2015, MNRAS, 454, 4335
Beltrán, M. T., Rivilla, V. M., Kumar, M. S. N., Cesaroni, R., & Galli, D. 2022, A&A, 660, L4
Berry, D. S., Reinhold, K., Jenness, T., & Economou, F. 2007, in ASP Conf. Ser. 376, Astronomical Data Analysis Software and Systems XVI, ed. R. A. Shaw, F. Hill, & D. J. Bell (San Francisco, CA: ASP), 425
Beuther, H., Churchwell, E. B., McKee, C. F., & Tan, J. C. 2007, in Protostars and Planets V, ed. V. B. Reipurth, D. Jewitt, & K. Keil (Tucson, AZ: Univ. Arizona Press)
Blitz, L., Fich, M., & Stark, A. A. 1982, ApJS, 49, 183
Bolatto, A. D., Wolfire, M., & Leroy, A. K. 2013, ARA&A, 51, 207
Bronfman, L., Nyman, L. A., & May, J. 1996, A&AS, 115, 81
Brunt, C. M., Kerton, C. R., & Pomerleau, C. 2003, ApJS, 144, 47
Buckle, J. V., Curtis, E. I., Roberts, J. F., et al. 2010, MNRAS, 401, 204
Buckle, J. V., Hills, R. E., Smith, H., et al. 2009, MNRAS, 399, 1026
Burov, A. B., Kislyakov, A. G., Krasilnikov, A. A., et al. 1988, SvAL, 14, 209
Calzetti, D. 2013, in Secular Evolution of Galaxies, ed. J. Falcón-Barroso & J. H. Knapen (Cambridge: Cambridge Univ. Press), 419
Cesaroni, R., Palagi, F., Felli, M., et al. 1988, A&AS, 76, 445
Condon, J. J., Cotton, W. D., Greisen, E. W., et al. 1998, AJ, 115, 1693
Currie, M. J., Berry, D. S., Jenness, T., et al. 2014, in ASP Conf. Ser. 485, Astronomical Data Analysis Software and Systems XXIII, ed. N. Manset & P. Forshay (San Francisco, CA: ASP), 391
Davis, C. J., Chrysostomou, A., Hatchell, J., et al. 2010, MNRAS, 405, 759
Deharveng, L., Zavagno, A., Nadeau, D., Caplan, J., & Petit, M. 1999, A&A, 344, 943
Dewangan, L. K., Ojha, D. K., & Baug, T. 2017a, ApJ, 844, 15

Dewangan, L. K., Ojha, D. K., Zinchenko, I., Janardhan, P., & Luna, A. 2017b, ApJ, 834, 22
Dewangan, L. K., Ojha, D. K., Luna, A., et al. 2016, ApJ, 819, 66
Dewangan, L. K., Ojha, D. K., Sharma, S., et al. 2020, ApJ, 903, 13
Dickinson, D. F., Frogel, J. A., & Persson, S. E. 1974, ApJ, 192, 347
Enoch, M. L., Evans, N. J. I., Sargent, A. I., et al. 2008, ApJ, 684, 1240
Enoch, M. L., Young, K. E., Glenn, J., et al. 2006, ApJ, 638, 293
Fich, M. 1993, ApJS, 86, 475
Fiege, J. D., & Pudritz, R. E. 2000, MNRAS, 311, 85
Fish, V. L. 2007, in IAU Symp. 242, Astrophysical Masers and Their Environments, ed. J. M. Chapman & W. A. Baan (Cambridge: Cambridge Univ. Press), 71
Fukui, Y., Habe, A., Inoue, T., Enokiya, R., & Tachihara, K. 2021, PASJ, 73, S1
Fuller, G. A., & Myers, P. C. 1992, ApJ, 384, 523
Ginsburg, A., Glenn, J., Rosolowsky, E., et al. 2013, ApJS, 208, 14
Goldsmith, P. F. 2001, ApJ, 557, 736
Graves, S. F., Richer, J. S., Buckle, J. V., et al. 2010, MNRAS, 409, 1412
Griffin, M. J., Abergel, A., Abreu, A., et al. 2010, A&A, 518, L3
Habe, A., & Ohta, K. 1992, PASJ, 44, 203
Hacar, A., Alves, J., Burkert, A., & Goldsmith, P. 2016, A&A, 591, A104
Hacar, A., Clark, S., Heitsch, F., et al. 2022, arXiv:2203.09562
Harju, J., Walmsley, C. M., & Wouterloot, J. G. A. 1993, A&AS, 98, 51
Hennemann, M., Motte, F., Schneider, N., et al. 2012, A&A, 543, L3
Heyer, M. H., Brunt, C., Snell, R. L., et al. 1998, ApJS, 115, 241
Hildebrand, R. H. 1983, QJRAS, 24, 267
Inoue, T., & Fukui, Y. 2013, ApJL, 774, L31
Inutsuka, S.-i., & Miyama, S. M. 1997, ApJ, 480, 681
Johansson, L. E. B., Olofsson, H., Hjalmarson, A., Gredel, R., & Black, J. H. 1994, A&A, 291, 89
Kerton, C. R., & Brunt, C. M. 2003, A&A, 399, 1083
Koumpia, E., Harvey, P. M., Ossenkopf, V., et al. 2015, A&A, 580, A68
Krumholz, M. R., & McKee, C. F. 2020, MNRAS, 494, 624
Kumar, M. S. N., Arzoumanian, D., Men'shchikov, A., et al. 2022, A&A, 658, A114
Kumar, M. S. N., Keto, E., & Clerkin, E. 2006, A&A, 449, 1033
Kumar, M. S. N., Palmeirim, P., Arzoumanian, D., & Inutsuka, S. I. 2020, A&A, 642, A87
Kurtz, S. 2002, in ASP Conf. Ser. 267, Hot Star Workshop III: The Earliest Phases of Massive Star Birth, ed. P. A. Crowther (San Francisco, CA: ASP), 81
Lada, C. J., Bergin, E. A., Alves, J. F., & Huard, T. L. 2003, ApJ, 586, 286
Lada, C. J., & Fich, M. 1996, ApJ, 459, 638
Li, Y., Calzetti, D., Kennicutt, R. C., et al. 2010, ApJ, 725, 677
Longmore, S. N., Kruijssen, J. M. D., Bastian, N., et al. 2014, in Protostars and Planets VI, ed. H. Beuther et al. (Tucson, AZ: Univ. Arizona Press), 291
Mallick, K. K., Kumar, M. S. N., Ojha, D. K., et al. 2013, ApJ, 779, 113
Mallick, K. K., Ojha, D. K., Tamura, M., et al. 2015, MNRAS, 447, 2307
Marsh, K. A., Whitworth, A. P., & Lomax, O. 2015, MNRAS, 454, 4282
Marsh, K. A., Whitworth, A. P., Lomax, O., et al. 2017, MNRAS, 471, 2730
Martín-Hernández, N. L., Peeters, E., Morisset, C., et al. 2002, A&A, 381, 606
Men'shchikov, A. 2021, A&A, 649, A89
Molinari, S., Swinyard, B., Bally, J., et al. 2010, PASP, 122, 314
Moran, J. M. 1983, RMxAA, 7, 95
Motte, F., Bontemps, S., & Louvet, F. 2018, ARA&A, 56, 41
Myers, P. C. 2009, ApJ, 700, 1609
Palagi, F., Cesaroni, R., Comoretto, G., Felli, M., & Natale, V. 1993, A&AS, 101, 153
Panagia, N. 1973, AJ, 78, 929
Peretto, N., Fuller, G. A., André, P., et al. 2014, A&A, 561, A83
Poglitsch, A., Waelkens, C., Geis, N., et al. 2010, A&A, 518, L2
Portegies Zwart, S. F., McMillan, S. L. W., & Gieles, M. 2010, ARA&A, 48, 431
Priestley, F. D., & Whitworth, A. P. 2021, MNRAS, 506, 775
Qin, S.-L., Wang, J.-J., Zhao, G., Miller, M., & Zhao, J.-H. 2008, A&A, 484, 361
Ragan, S. E., Henning, T., Tackenberg, J., et al. 2014, A&A, 568, A73
Ridge, N. A., & Moore, T. J. T. 2001, A&A, 378, 495
Rosolowsky, E., Dunham, M. K., Ginsburg, A., et al. 2010, ApJS, 188, 123
Scoville, N. Z., Sanders, D. B., & Clemens, D. P. 1986, ApJL, 310, L77
Shirley, Y. L. 2015, PASP, 127, 299
Slysh, V. I., Val'tts, I. E., Kalenskii, S. V., et al. 1999, A&AS, 134, 115
Szymczak, M., Hrynek, G., & Kus, A. J. 2000, A&AS, 143, 269
Takahira, K., Tasker, E. J., & Habe, A. 2014, ApJ, 792, 63
Tan, J. C. 2000, ApJ, 536, 173
Taylor, A. R., Gibson, S. J., Peracaula, M., et al. 2003, AJ, 125, 3145
Treviño-Morales, S. P., Fuente, A., Sánchez-Monge, Á., et al. 2019, A&A, 629, A81
Urquhart, J. S., Morgan, L. K., Figura, C. C., et al. 2011, MNRAS, 418, 1689
Vázquez-Semadeni, E., Palau, A., Ballesteros-Paredes, J., Gómez, G. C., & Zamora-Avilés, M. 2019, MNRAS, 490, 3061
Williams, G. M., Peretto, N., Avison, A., Duarte-Cabral, A., & Fuller, G. A. 2018, A&A, 613, A11
Williams, J. P., de Geus, E. J., & Blitz, L. 1994, ApJ, 428, 693
Wouterloot, J. G. A., & Brand, J. 1989, A&AS, 80, 149
Wouterloot, J. G. A., Brand, J., & Fiegle, K. 1993, A&AS, 98, 589
Yoo, H., Kim, K.-T., Cho, J., et al. 2018, ApJS, 235, 31
Yuan, J., Li, J.-Z., Wu, Y., et al. 2018, ApJ, 852, 12
Zhang, J. S., Liu, W., Yan, Y. T., et al. 2020, ApJS, 249, 6
Zinchenko, I. I., Krasilnikov, A. A., Kukina, E. P., Lapinov, A. V., & Pirogov, L. E. 1990, SvA, 34, 458
Zinchenko, I. I., Liu, S.-Y., Su, Y.-N., Wang, K.-S., & Wang, Y. 2020, ApJ, 889, 43
Zinnecker, H., & Yorke, H. W. 2007, ARA&A, 45, 481
Zucker, C., Battersby, C., & Goodman, A. 2018, ApJ, 864, 153